

1. Introduction. Southern California has a long history of seismic imaging studies at all scales, from regional tomography (e.g., Fang et al., 2016; Lee et al., 2014; Qiu et al., 2019; Tape et al., 2009), to local-scale basin and fault-zone structure (e.g., Allam et al., 2014; Fuis et al., 2001, 2017; Süß & Shaw, 2003), and multi-scale joint inversions of multiple datasets (Berg et al., 2018; Bennington et al., 2015). A primary motivation for these works is the significant seismic hazard posed by the San Andreas fault system, and the related need for physics-based hazard assessment of the region (Graves et al., 2011; Vidale & Helmberger, 1988). For the past 25 years, the Southern California Earthquake Center has developed and maintained multiple Community Velocity Models (CVM) with seismic hazard assessment as one of the explicit goals (Chen et al., 2007; Lee et al., 2014; Magistrale et al., 1996; Plesch et al., 2007; Süß & Shaw, 2003; Tape et al., 2009). Despite the long history and contributions from a large community of researchers, there are still several shortcomings to the Southern California CVM. In particular, near-surface velocity structure (<1km depth), and corresponding ratio of compressional to shear velocity (V_p/V_s), remain poorly resolved at regional scales. Shallow structure is well-known to exert strong influence on the co-seismic ground motion (e.g., Graves et al., 2011), while local V_p/V_s ratio can produce amplification by a factor of three (Yang & Sato, 2000) even for sites already subject to amplification due to low local shear wave velocity (e.g., basins). To address these issues, several versions of the CVM (Lee et al., 2014; Plesch et al., 2007) include a shallow layer constrained by very local-scale geotechnical studies; this ad hoc layer creates various edge effects and other artifacts in the model and wavefield simulations (Taborda et al., 2016).

Measurements of V_p/V_s for southern California generally fall into three categories: low-resolution volumetric averages (e.g., Allam et al., 2014; Hauksson, 2000; Lin et al., 2007), localized measurements at seismogenic depth (e.g., Lin & Shearer, 2007; Lin, 2020; Zhang & Lin, 2014), and localized near-surface measurements from boreholes (Boore et al., 2003; Shaw et al., 2015 and references therein) or temporary seismic arrays (e.g., Murphy et al., 2010). The latter category is the most important for seismic hazard, but the extremely local nature is difficult to implement in physics-based assessments. Though there are many models which independently constrain V_p and/or V_s (e.g., Lee et al., 2014; Lin et al., 2010; Schmandt & Humphreys, 2010; Tanimoto & Sheldrake, 2002), naïvely dividing V_p by V_s models obtained with different data of differing resolution results in extreme inaccuracies and numerical artifacts (e.g., Allam & Ben-Zion, 2012). In addition, because most methods measure V_p/V_s at depth from earthquake sources, they lead to overestimations of V_p/V_s ratio under near-surface stress conditions (Zaitsev et al., 2017).

In order to provide a model with resolution of V_s and V_p/V_s in the upper few km, we combine the complementary sensitivities of Rayleigh-wave phase velocities (upper crust), ellipticity (upper few km), and the initial pulse of teleseismic receiver functions (shallow V_p/V_s ratio and shallow interfaces) to create a self-consistent model at the regional scale across southern California. The idea to combine receiver functions and surface wave data in a Bayesian joint inversion to determine V_s and V_p/V_s is relatively new (Dreiling et al., 2020; Ojo et al., 2019), and only recently shown to be promising in resolving near-surface V_s and V_p/V_s in sediments (Li et al., 2019). By including V_p/V_s as a parameter we are able to fit receiver functions on a regional scale for the first time across 231 Southern California stations, including in basins where receiver functions have long been discarded as nuisance signals or “corrected” with ad-hoc models, as reverberations overprint Moho and other crustal signatures (e.g., Yeck et al., 2013). The results, presented in Section 3 and discussed in Section 4 below, include a map of V_p/V_s across the region and 3D shear-velocity (V_s) model with very low near-surface velocities in basins more in line with previous measurements of shallow, local V_s .

2. Data and Methods

2.1 Ambient Noise Surface Wave Measurements. We process three-component broadband stations identically to Berg et al. (2018), except to apply an initial band-pass filter to all continuous recordings of 0.5 to 170 s periods (instead of 5 to 150 s) to avoid frequency-band edge effects. We retain relative amplitude information during cross-correlation to measure Rayleigh-wave ellipticity, or horizontal-to-vertical (H/V) ratios (Berg et al., 2018; Lin et al., 2014). The isotropic H/V ratio and uncertainty are determined from the mean and standard deviation of the mean, respectively, for each station with at least 20 measurements remaining after removing outliers; more details can be found in Berg et al. (2018). In addition to Rayleigh-wave H/V ratio measurements from 6 to 10 s periods, we use 3 to 10 s periods Rayleigh-wave phase velocities from previous ambient-noise-based eikonal tomography (Qiu et al., 2019) extracted at the inversion grid point nearest to each station.

2.2 Receiver Functions. We obtain receiver functions, which capture near-station structural contrasts via P to S conversions and reverberations (Langston, 1977; Ligorria & Ammon, 1999; Vinnik, 1977). We analyze P and P_{diff} arrivals and their coda from all teleseismic events from January 2004 to August 2020 with $M_w > 5.1$ and epicentral distances 28° to 150° via the time domain iterative method of Ligorria and Ammon (1999) with a Gaussian filter factor of 3. We apply automated processing based on previous work (Schulte-Pelkum & Mahan, 2014a; 2014b) including basic quality control steps, correction to a standard ray parameter of 0.06 s/km, and receiver function binning by back-azimuth; see Schulte-Pelkum & Mahan (2014a; 2014b) for details. The final isotropic receiver function consists of the mean of all back-azimuths for stations with a minimum of 14 individual receiver functions. To focus on shallow structure, we only consider the first 2 s of each receiver function. In sedimentary basins the initial pulse is delayed due to the superposition of direct P and larger amplitude sediment P_s conversions, as the large velocity contrast at the sediment base refracts rays to nearly-vertical incidence (Li et al., 2019; Schulte-Pelkum et al., 2017). Larger delay times of the initial receiver function pulse are clearly observed in basin stations.

2.3 Monte Carlo Joint Inversion. We leverage the complementary sensitivities of the Rayleigh phase velocity, H/V ratio, and receiver function datasets through a Markov Chain Monte Carlo (MCMC) joint inversion at each station to fully explore the parameter space, quantify model uncertainty, and avoid local minima (Berg et al., 2018; Roy & Romanowicz, 2017; Shen & Ritzwoller, 2016). Our MCMC model for each station consists of a top linear layer over a crustal layer with initial V_s from Berg et al. (2018) and initial V_p/V_s from the Brocher (2005) empirical relationship. Crustal V_s is parameterized with ten cubic B-splines with asymmetric density higher in the shallower crust (Berg et al., 2018). We perturb eight free parameters (**Table S1**), including the V_s in the top linear layer and the upper four B-splines in the crust, as well as the thickness and V_p/V_s in the top linear layer. The a priori distribution is formed by Gaussian probability with empirically chosen widths to fully sample the model space (see **Table S1**). We impose three prior constraints: a maximum V_s of 4.9 km/s, a positive jump from the bottom of the top linear layer into the crustal layer, and a V_p/V_s ratio greater than 1.

The inversion explores the a priori distribution following the Metropolis algorithm (Shen et al., 2012) with misfit characterized as root-mean-square between data and model predictions with empirically chosen weights of 30%, 30%, and 40% for phase velocities, H/V ratios, and receiver functions respectively. Models with misfit less than 1.5 of the minimum misfit are included in the posterior distribution, and we require the posterior to contain more than 300 models for the station to be included in the final results. On average, there are ~2000 models in each posterior. Details about the number of iterations, avoiding the edges of

prior distributions, and data uncertainties can be found in previous works (Berg et al., 2018, 2020; Shen et al., 2012).

Our final model is formed by the mean of the model parameters in the posterior, except in cases where the mean results in a misfit value higher than that in the posterior (i.e., higher than 1.5 times the absolute minimum misfit). This generally occurs where the posterior models have bimodal distribution, and in these instances our final model is the model with minimum misfit.

Fig. 1 shows the 1-D inversion result for station RUS, including the full prior and posterior distributions and data fits, and the effects of the inclusion of the receiver function data. When the receiver function data (**Fig. 1c**) are not used, the shallow structure and V_p/V_s ratio (**Fig. 1a, 1b**) are poorly constrained by the inversion, though the Rayleigh wave ellipticity and phase velocity (**Fig. 1d, 1e**) are equally well-fit in either case. By incorporating receiver functions, not only do we gain better constraint on the near-surface layered interface structure (Allam et al., 2017; Langston, 1979; Shen & Ritzwoller, 2016; Ward & Lin, 2018), but the complementary dataset results in a tighter distribution of results in both the V_s and the V_p/V_s model space (**Fig. 1a, 1b**). Thus receiver function data are most sensitive to the near-surface velocity and V_p/V_s ratio, justifies the inclusion of the latter, and demonstrates receiver function utility when included in this inversion.

3. Results

3.1 Rayleigh-Wave Ellipticity and Receiver Function Measurements. As in previous work (Berg et al., 2018), at 7 s period we observe high H/V ratios in sedimentary basins including the Los Angeles, Central Valley, Salton Trough, and Ventura basins; we observe low H/V ratios in mountainous regions such as the Sierra Nevada and Peninsular Ranges. The surface patterns of soft sediment compared to hard bedrock are also evident from the Wills & Clahan (2006) V_s30 map of the region.

From the map of receiver function initial pulse delay time, we see similar patterns to those of the H/V ratio map and the V_s30 map. We observe earlier arrivals of the initial receiver function pulse in crystalline rock, including in the Peninsular and Sierra Nevada Ranges, and later arrivals in sedimentary basins, including the Los Angeles basin and the Salton Trough. The superposition of direct P and larger amplitude P-to-S conversions in sedimentary basins, from the bedrock interface and reverberations within, yields delayed and more-intricate initial pulses in the receiver functions (Li et al., 2019; Schulte-Pelkum et al., 2017; Yeck et al., 2013). Although typically ignored for their complexity (e.g., Allam et al., 2017), we directly compare the receiver function delay times to the short-period H/V ratios as both have shallow sensitivity. We observe strong correlation values (mean correlation coefficient 0.76) between 6-10 s period H/V ratios and receiver function delay times; higher H/V ratios correspond to later receiver function initial pulse times, which in turn correspond to lower V_s30 areas.

3.2 Shear Velocity Model. **Figs 2a** and **2b** show the V_s velocity MCMC inversion result at 0 km and 1 km depths, respectively, interpolated onto the underlying map, with a cross-section shown in **Fig. 2d**. Major features include low- V_s sedimentary basins such as the Los Angeles basin, Central Valley, Ventura basin, and Salton Trough. We also observe the high- V_s Peninsular and Sierra Nevada Ranges. Less prominent features include the Indian Wells Valley (**Figs 2a** and **2b**) east of the Sierra Nevada, shallow Antelope Valley (**Fig. 2a**) in the northwest corner of the Mojave desert, and the low- V_s Coast Ranges (**Fig. 2a**). The northwest section of the Eastern California Shear Zone (ECSZ; **Fig. 2a**) is observed as a broad low velocity zone at the surface, and strong across-fault contrasts in velocity are observed on the southern San Andreas, San Jacinto, and Elsinore faults (**Figs 2a** and **2b**). In comparison to our previous Berg et al. (2018) model (i.e., our starting model), we have stronger constraint to the near-surface with V_s values slower in areas of soft sediments (e.g.,

Salton Trough, LA and Central Valley basins) and faster in regions of crystalline rock (e.g., Sierra Nevada and Peninsular Ranges). A direct comparison of starting (red triangles, **Fig. 1a**) to final model (yellow squares, **Fig. 1a**), shows that the most prominent changes occur in the upper few km.

In **Fig. 2c** we show depth to Vs of 3km/s as an approximate basin depth map, based on the empirical Vp/Vs relationship (Brocher, 2005) and previous observations in the LA basin (Süss & Shaw, 2003). We observe a greater depth to 3km/s in the southeast portion of the LA and Ventura basins, and mid-range depths for the Central Valley and in the Salton Trough. This agrees with previous studies (Berg et al., 2018; Fletcher & Erdem, 2017; Flidner et al., 2000; Fuis et al., 2017; Han et al., 2016; Livers et al., 2012; Ma & Clayton, 2016; Magistrale et al., 1996). The Antelope Valley and Indian Wells Valley are shallower, fitting previous active-source studies (Lutter et al., 2004; Tape et al., 2010).

3.3 Vp/Vs in the Near Surface. While Vp/Vs in the top linear layer is resolved for every station, we analyze only those stations with a prominent layer thickness (>0.75 km) and with low normalized standard deviation of the Vp/Vs in the posterior (<0.15) to avoid including less reliable results. **Fig. 3a** shows the Vp/Vs at stations satisfying these criteria, and the interpolated map. **Fig. 3b** shows a scatter plot of the top linear layer average Vs compared to Vp/Vs value (circles) and the Brocher (2005) estimate (line). We observe high scatter around the Brocher-predicted Vp/Vs value skewed towards lower Vp/Vs (**Fig. 3b**), particularly for areas with higher Vs values.

We observe higher Vp/Vs in the Salton Trough, eastern LA basin, Central Valley, Indian Wells Valley, Antelope Valley, and in the ESCZ with corresponding slower sediments. We observe lower Vp/Vs in the Sierra Nevada mountains, in the center of the Mojave desert, and in the Peninsular Ranges. Additionally, we see a transition from higher Vp/Vs near the San Andreas fault to low Vp/Vs along the San Jacinto and Elsinore faults. These observations are consistent with previous studies (Fang et al., 2019; Lin et al., 2007), and discussed in detail in the following section.

4. Discussion

4.1 Mountains and Mojave Desert. Compared to Berg et al. (2018), we observe faster near-surface Vs values in the Sierra Nevada and Peninsular Ranges (**Fig.s 2a-b**), similar to the CVMS geotechnical layer (GTL) (Shaw et al., 2015). Though the Vp/Vs ratio of rocks can vary significantly with fluid content and fracture density (Shearer, 1988; Karato & Jung, 1998), Christensen (1996) suggests that composition controls the general properties of igneous rock; felsic (e.g., granite) rocks have relatively low Vp/Vs ratio (<1.7) and high silica content ($>65\%$), while mafic (e.g., basalt) rocks have higher Vp/Vs ratios (>1.8) and lower silica content ($<45\%$). In the Sierra Nevada Range, we observe lower Vp/Vs consistent with Cretaceous granitic rocks (Irwin, 1990) at the surface and previous studies (Hauksson, 2000; Lin et al., 2007; Murphy et al., 2010). Consistent to previous studies (Fang et al., 2019; Hauksson, 2000), we resolve, in the southernmost portion of our study, the northern extent of the complex mafic Peninsular Ranges batholith containing an abundance of gabbros (Gastil et al., 1975; Hauksson, 2000; Kimbrough & Grove, 2005; Langenheim & Jachens, 2000; Wetmore et al., 2003) with corresponding relatively higher (~ 1.8) Vp/Vs ratios. We also observe the transition to the northeast into more quartz-rich granitic material (Gastil et al., 1975; Hauksson, 2000; Kimbrough & Grove, 2005; Wetmore et al., 2003), including into the fast-Vs low-Vp/Vs Cretaceous plutons (Morton & Kennedy, 2005) between the Elsinore and San Jacinto faults. Relatively low Vp/Vs ratios in the Mojave Desert between Antelope Valley (previously observed by Hauksson, 2000 & Murphy et al., 2010) and the ECSZ likely correspond to Precambrian metamorphic and plutonic rocks with values consistent to lab measurements (McCaffree Pellerin & Christensen, 1998).

Similar to previous studies, we observe higher Vp/Vs (**Fig. 3a**) in portions of the San Andreas fault (Fang et al., 2019; Murphy et al., 2010) and in the ECSZ (Hauksson, 2000; Lin et al., 2007) where slower Vs is also observed (**Fig. 2a**). S-waves are particularly sensitive to reduction in velocity within a fault damage zone due to the high fracture density (Catchings et al., 2014, 2020; Mitchell & Faulkner, 2009), as observed along the Mojave section of the San Andreas Fault (Fang et al., 2019; Murphy et al., 2010). Similarly, the ECSZ contains low-Vs and high-Vp/Vs which we interpret as widespread aligned fractures created by the broad region of strike-slip deformation (Sauber et al., 1986).

More generally in our model, stations outside of sedimentary basins have low Vp/Vs (< 1.75) ratios (**Figs 3a and 3b**). While these values are lower than anticipated from previous imaging (Hauksson, 2000) and laboratory (Christensen, 1996) studies, recent work (Zaitsev et al., 2017) shows that low Vp/Vs and a negative Poisson ratio (Vp/Vs < 1.42) is not an exotic result and has been observed in a significant portion of experimental data samples (~45%) at low confining stress (i.e., surface conditions). Previous southern California imaging studies have observed higher Vp/Vs ratios likely due to greater depth sensitivity (Hauksson, 2000; Lin & Shearer, 2007; Lin et al., 2007). The low Vp/Vs ratios obtained in the present model suggest widespread fracturing and/or poor consolidation with little-to-no fluid saturation (Avseth & Bachrach, 2005; Bachrach et al., 2000; Shearer, 1988) in the near-surface crust of Southern California outside of major basins.

4.2 Basins. Major basins in Southern California are clearly observed as regions of high Vp/Vs and reduced Vs (**Fig. 2a**), lower than previous imaging work (Berg et al., 2018; Lee et al., 2014; Tape et al., 2010) and more in line with estimates of Vs30/GTL (Shaw et al., 2015). These include the Salton Trough, Central Valley, and Los Angeles and Ventura basins. We do not observe the San Bernardino Basin – likely because of station coverage and overall shallow basement depth (Anderson et al., 2004) – but the nearby Cajon and Banning Passes are visible as low-Vs high-Vp/Vs areas.

The high Vp/Vs ratios (**Fig. 3a**) seen in all basins are consistent with fluid-saturated measurements and observed in previous studies (Fang et al., 2019; Hauksson, 2000; Hauksson & Haase, 1997; Lin et al., 2007; Murphy et al., 2010). In the LA basin we observe strong similarities in Vs to the GTL, which is well-constrained via dense borehole measurements (Shaw et al., 2015). Although we have limited horizontal resolution due to station coverage, we observe that the deepest part of the LA basin (**Fig. 2c**) lies between the Newport-Inglewood and Whittier faults (20-50km distance in **Fig. 2d**). This portion of the LA basin coincides with relatively higher Vp/Vs ratios, potentially related to the shallower water table (CA DWR, 2017; WRD, 2017), and is consistent to previous studies based on borehole measurements (Hauksson & Haase, 1997) and local earthquakes (Lin et al., 2007). North of the Hollywood fault, in the Santa Monica mountains between the LA and Ventura basins, we observe low Vp/Vs similar to borehole studies (Hauksson & Haase, 1997). The Santa Monica mountains contain Mesozoic igneous and metamorphic granitic rocks (Lutter et al., 2004; Murphy et al., 2010), and the region adjacent to the Hollywood fault contains granitic and dioritic plutonic rocks (Hildenbrand et al., 2001).

5. Conclusions. We apply Markov Chain Monte Carlo inversion of short-period Rayleigh-wave phase velocity and ellipticity with early-time (0-2 s) receiver functions to determine shallow Vs (<10 km) and near-surface Vp/Vs ratios. We observe Vs values near the surface that more closely resemble borehole and exploration studies in the Los Angeles basin, and higher Vs in the Peninsular and Sierra Nevada Ranges near the surface. Our low Vp/Vs ratio results outside of fluid-saturated basins correspond to mafic material in the Peninsular Ranges, felsic material in the Sierra Nevada Ranges and granitic regions, and significantly overall low Vp/Vs suggests widespread shallow fracturing and/or groundwater undersaturation.

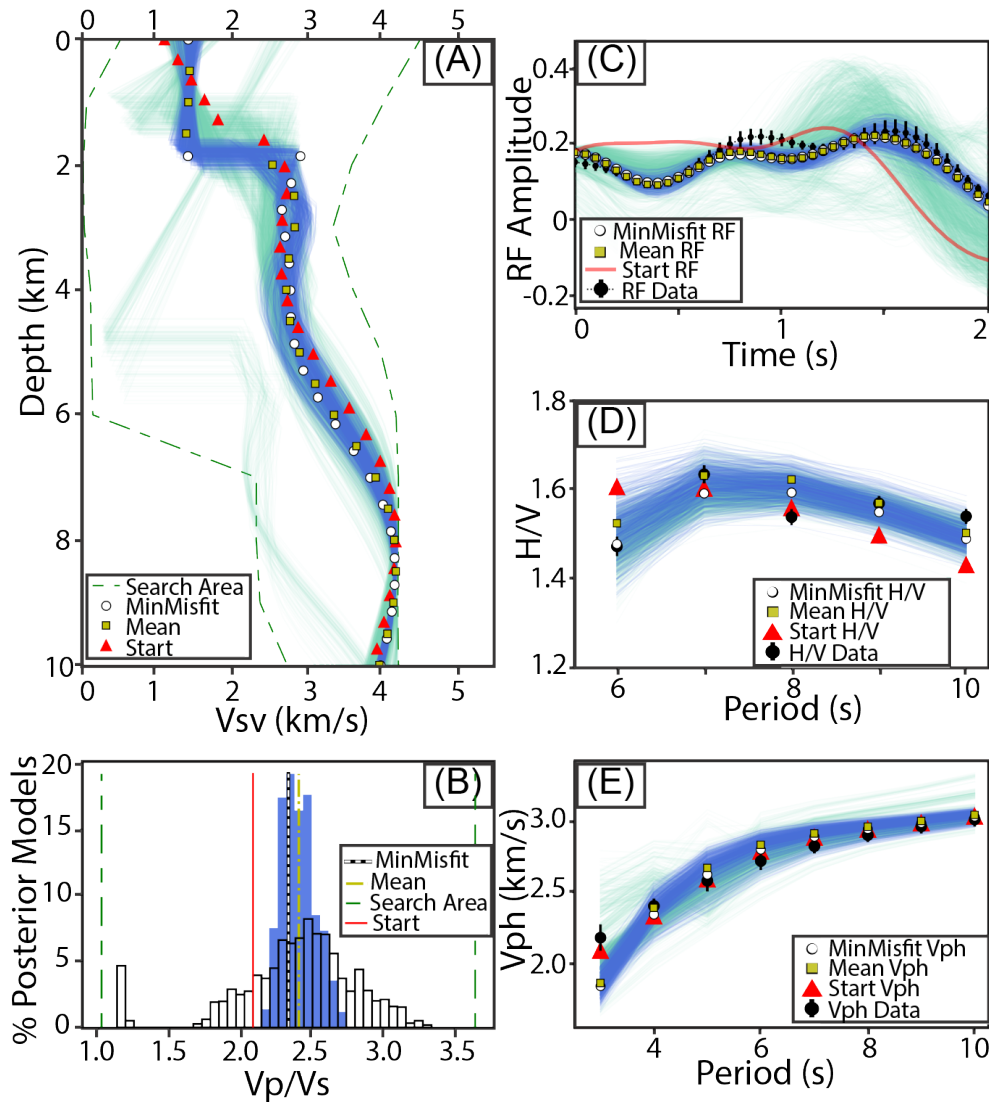


Figure 1. MCMC joint inversion results for station RUS including (a-b) search area (green dashed lines), posterior results when incorporating Rayleigh-wave phase velocity and H/V data only ((a) light green or (b) transparent) and all datasets (blue), as well as the starting model (red), minimum misfit model from the posterior (white), and mean model from the posterior (yellow) for both (a) shear velocity (V_s) results of the top 10km and (b) V_p/V_s results of the top linear layer. Data (black) and forward model results for the posterior sets, starting, mean, and minimum misfit models for (c) receiver functions, (d) H/V, and (e) phase velocities.

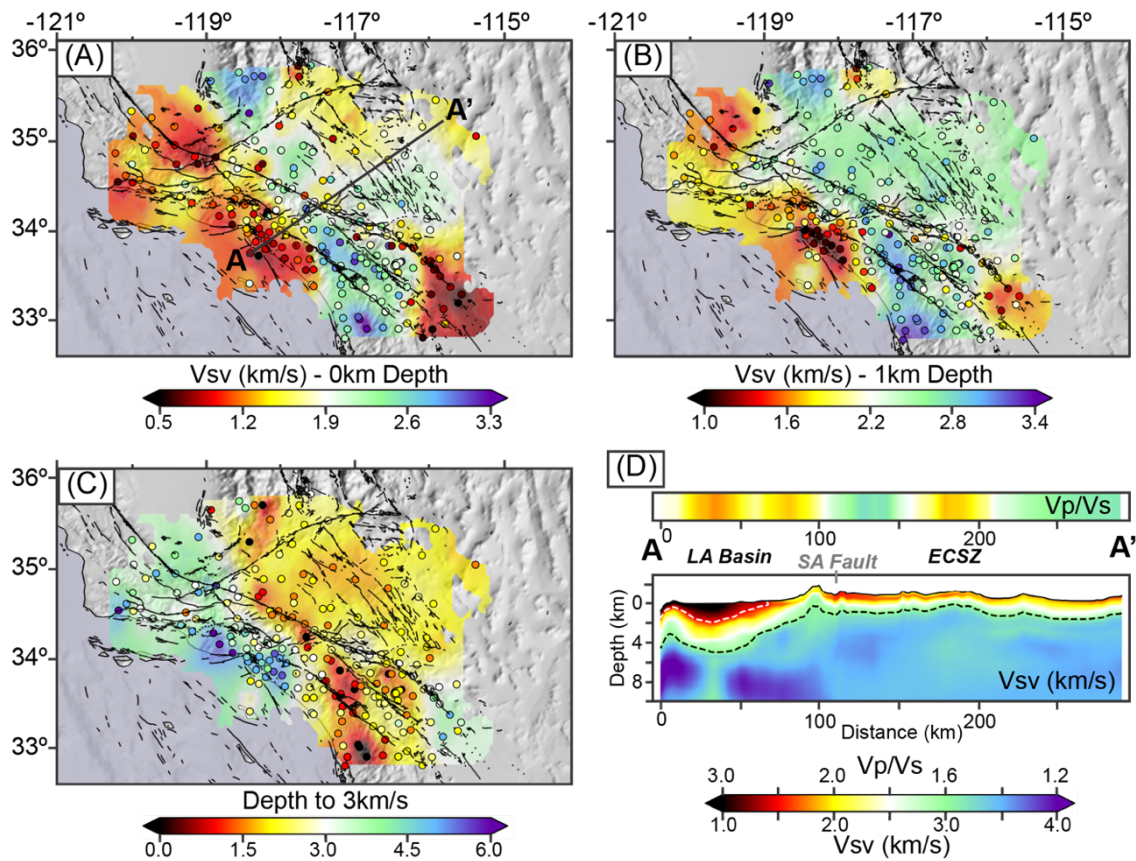


Figure 2. Vs results at each station, with Gaussian-smoothed underlying map, at (a) the surface and (b) 1 km depths, and (c) depth to 3 km/s. (d) Cross-section A-A' for Vp/Vs ratio in the top linear layer (top) and Vs to 10 km depth (bottom), including white dashed line at 1.5 km/s and black dashed line at 3 km/s.

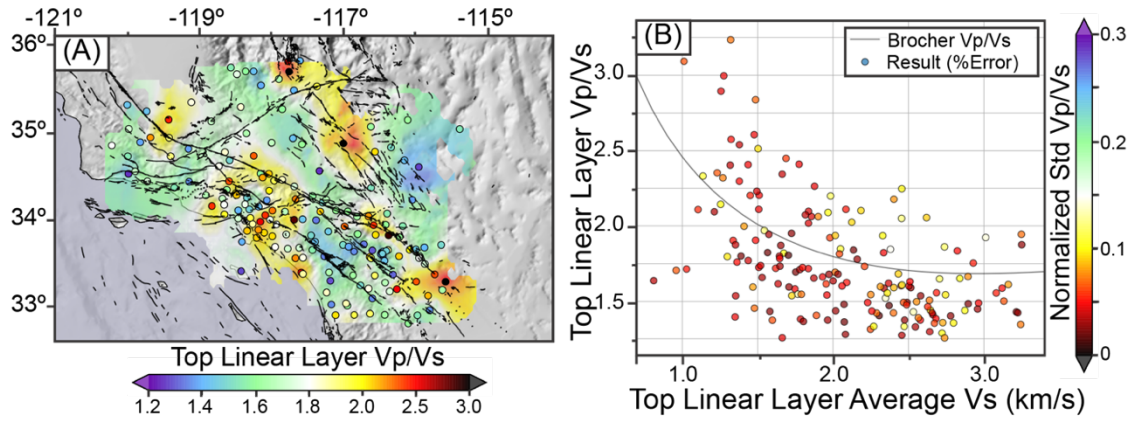


Figure 3 Vp/Vs results from the top linear layer as a (a) map at each station, with Gaussian-smoothed underlying map, and (b) scatter plot from each station of average Vs in the top linear layer versus Vp/Vs of the top linear layer.

Table S1. Prior Distributions in the Joint Inversion

Parameter	Range	Gaussian ½-Width
Top Linear Layer Thickness	$m_0 \pm 5$	0.1
Vsv, Top of Top Linear Layer (km/s)	$m_0 \pm 4$	0.05
Vsv, Bottom of Top Linear Layer	$m_0 \pm 4$	0.05
Vp/Vs in Top Linear Layer	$m_0 \pm 0.75 m_0$	0.05
Crust, 1 st -4 th (of 10) B-splines (km/s)	$m_0 \pm 0.2 m_0$	0.05

Note. (left) A full list of the 8 inversion parameters, (middle) the ranges explored with m_0 as the starting model value, and (right) the Gaussian half-width that defines the a priori distributions.

References

- Allam, A. A., & Ben-Zion, Y. (2012). Seismic velocity structures in the Southern California plate boundary environment from double-difference tomography. *Geophysical Journal International*, *190*(2), 1181–1196. <https://doi.org/10.1111/j.1365-246X.2012.05544.x>
- Allam, A. A., Ben-Zion, Y., Kurzon, I., & Vernon, F. (2014). Seismic velocity structure in the hot springs and trifurcation areas of the San Jacinto fault zone, California, from double-difference tomography. *Geophysical Journal International*, *198*(2), 978–999. <https://doi.org/10.1093/gji/ggu176>
- Allam, A. A., Schulte-Pelkum, V., Ben-Zion, Y., Tape, C., Ruppert, N., & Ross, Z. E. (2017). Ten kilometer vertical Moho offset and shallow velocity contrast along the Denali fault zone from double-difference tomography, receiver functions, and fault zone head waves. *Tectonophysics*, *721*, 56–69. <https://doi.org/10.1016/j.tecto.2017.09.003>
- Anderson, M., Matti, J., & Jachens, R. (2004). Structural model of the San Bernardino basin, California, from analysis of gravity, aeromagnetic, and seismicity data. *Journal of Geophysical Research: Solid Earth*, *109*(B4). <https://doi.org/10.1029/2003JB002544>.
- Avseth, P., & Bachrach, R. (2005). Seismic properties of unconsolidated sands: Tangential stiffness, V_p/V_s ratios and diagenesis. In *SEG Technical Program Expanded Abstracts 2005* (pp. 1473-1476). Society of Exploration Geophysicists. <https://doi.org/10.1190/1.2147968>
- Bachrach, R., Dvorkin, J., & Nur, A. M. (2000). Seismic velocities and Poisson's ratio of shallow unconsolidated sands. *Geophysics*, *65*(2), 559-564. <https://doi.org/10.1190/1.1444751>
- Bennington, N. L., Zhang, H., Thurber, C. H., & Bedrosian, P. A. (2015). Joint inversion of seismic and magnetotelluric data in the Parkfield Region of California using the normalized cross-gradient constraint. *Pure and Applied Geophysics*, *172*(5), 1033-1052. <https://doi.org/10.1007/s00024-014-1002-9>
- Bensen, G. D., Ritzwoller, M. H., Barmin, M. P., Levshin, A. L., Lin, F., Moschetti, M. P., et al. (2007). Processing seismic ambient noise data to obtain reliable broad-band surface wave dispersion measurements. *Geophysical Journal International*, *169*(3), 1239–1260. <https://doi.org/10.1111/j.1365-246X.2007.03374.x>
- Berg, E. M., Lin, F. C., Allam, A., Qiu, H., Shen, W., & Ben-Zion, Y. (2018). Tomography of Southern California via Bayesian joint inversion of Rayleigh wave ellipticity and phase velocity from ambient noise cross-correlations. *Journal of Geophysical Research: Solid Earth*, *123*(11), 9933–9949. <https://doi.org/10.1029/2018JB016269>
- Berg, E. M., Lin, F.-C., Allam, A., Schulte-Pelkum, V., Ward, K. M., & Shen, W. (2020). Shear velocity model of Alaska via joint inversion of Rayleigh wave ellipticity, phase velocities, and receiver functions across the Alaska transportable Array. *Journal of Geophysical Research: Solid Earth*, *125*, e2019JB018582. <https://doi.org/10.1029/2019JB018582>

- Boore, D. M., Gibbs, J. F., & Rodriguez, M. (2003). *A compendium of P-and S-wave velocities from surface-to-borehole logging: Summary and reanalysis of previously published data and analysis of unpublished data* (p. 13). US Department of the Interior, US Geological Survey. <http://pubs.usgs.gov/of/2003/0191/>.
- Brocher, T. (2005). Empirical relations between elastic wavespeeds and density in the Earth's crust. *Bulletin of the Seismological Society of America*, 95(6), 2081–2092. <https://doi.org/10.1785/0120050077>
- California Department of Water Resources (2017), SGMA Portal –GSA Formation Notification System, State of California Department of Water Resources. <https://sgma.water.ca.gov/webgis/?appid=SGMADataViewer#gwlevels>
- Catchings, R. D., Rymer, M. J., Goldman, M. R., Sickler, R. R., & Criley, C. J. (2014). A method and example of seismically imaging near-surface fault zones in geologically complex areas using Vp, Vs, and their ratios. *Bulletin of the Seismological Society of America*, 104(4), 1989–2006. <https://doi.org/10.1785/0120130294>
- Catchings, R. D., Hernandez, J., Goldman, M. R., Chan, J. H., Sickler, R. R., Olson, B., & Criley, C. J. (2020). *2018 US Geological Survey–California Geological Survey Fault-Imaging Surveys Across the Hollywood and Santa Monica Faults, Los Angeles County, California* (No. 2020-1049). US Geological Survey. <https://doi.org/10.3133/ofr20201049>
- Chen, P., Zhao, L., & Jordan, T. H. (2007). Full 3D tomography for the crustal structure of the Los Angeles region. *Bulletin of the Seismological Society of America*, 97(4), 1094–1120. <https://doi.org/10.1785/0120060222>
- Christensen, N. I. (1996). Poisson's ratio and crustal seismology. *Journal of Geophysical Research: Solid Earth*, 101(B2), 3139–3156. <https://doi.org/10.1029/95JB03446>
- Dreiling, J., Tilmann, F., Yuan, X., Haberland, C., & Seneviratne, S. W. M. (2020). Crustal structure of Sri Lanka derived from joint inversion of surface wave dispersion and receiver functions using a Bayesian approach. *Journal of Geophysical Research: Solid Earth*, 125, e2019JB018688. <https://doi.org/10.1029/2019JB018688>
- Fang, H., Zhang, H., Yao, H., Allam, A., Zigone, D., Ben-Zion, Y., et al. (2016). A new algorithm for three-dimensional joint inversion of body wave and surface wave data and its application to the Southern California plate boundary region. *Journal of Geophysical Research: Solid Earth*, 121, 3557–3569. <https://doi.org/10.1002/2015JB012702>
- Fang, H., Yao, H., Zhang, H., Thurber, C., Ben-Zion, Y., & van der Hilst, R. D. (2019). Vp/Vs tomography in the southern California plate boundary region using body and surface wave traveltime data. *Geophysical Journal International*, 216(1), 609–620. <https://doi.org/10.1093/gji/ggy458>
- Fletcher, J. B., & Erdem, J. (2017). Shear-wave velocity model from Rayleigh wave group velocities centered on the Sacramento/San Joaquin Delta. *Pure and Applied Geophysics*, 174(10), 3825–3839. <https://doi.org/10.1007/s00024-017-1587-x>

- Fliedner, M. M., Klemperer, S. L., & Christensen, N. I. (2000). Three-dimensional seismic model of the Sierra Nevada arc, California, and its implications for crustal and upper mantle composition. *Journal of Geophysical Research*, *105*(B5), 10,899–10,921. <https://doi.org/10.1029/2000JB900029>
- Fuis, G. S., Ryberg, T., Godfrey, N. J., Okaya, D. A., & Murphy, J. M. (2001). Crustal structure and tectonics from the Los Angeles basin to the Mojave Desert, southern California. *Geology*, *29*(1), 15–18. [https://doi.org/10.1130/0091-7613\(2001\)0292.0.CO;2](https://doi.org/10.1130/0091-7613(2001)0292.0.CO;2)
- Fuis, G. S., Bauer, K., Goldman, M. R., Ryberg, T., Langenheim, V. E., Scheirer, D. S., et al. (2017). Subsurface geometry of the San Andreas Fault in Southern California: Results from the Salton Seismic Imaging Project (SSIP) and strong ground motion expectations. *Bulletin of the Seismological Society of America*, *107*(4), 1642–1662. <https://doi.org/10.1785/0120160309>
- Gastil, R. G., Phillips, R. P., & Allison, E. C. (1975). *Reconnaissance geology of the state of Baja California* (Vol. 140). Geological Society of America.
- Graves, R., Jordan, T. H., Callaghan, S., Deelman, E., Field, E., Juve, G., et al. (2011). CyberShake: A physics-based seismic hazard model for Southern California. *Pure and Applied Geophysics*, *168*(3–4), 367–381. <https://doi.org/10.1007/s00024-010-0161-6>
- Han, L., Hole, J. A., Stock, J. M., Fuis, G. S., Kell, A., Driscoll, N. W., et al. (2016). Continental rupture and the creation of new crust in the Salton Trough rift, Southern California and northern Mexico: Results from the Salton Seismic Imaging Project. *Journal of Geophysical Research: Solid Earth*, *121*, 7469–7489. <https://doi.org/10.1002/2016JB013139>
- Hauksson, E. (2000). Crustal structure and seismicity distribution adjacent to the Pacific and North America plate boundary in southern California. *Journal of Geophysical Research: Solid Earth*, *105*(B6), 13875–13903. <https://doi.org/10.1029/2000JB900016>
- Hauksson, E., & Haase, J. S. (1997). Three-dimensional VP and VP/VS velocity models of the Los Angeles basin and central Transverse Ranges, California. *Journal of Geophysical Research: Solid Earth*, *102*(B3), 5423–5453. <https://doi.org/10.1029/96JB03219>
- Herrmann, R. B., & Ammon, C. J. (2004). Surface waves, receiver functions and crustal structure, in Computer Programs in Seismology, Version 3.30, Saint Louis University. Retrieved from <http://www.eas.slu.edu/People/RBHerrmann/CPS330.html>
- Hildenbrand, T. G., Davidson, J. G., Ponti, D. J., & Langenheim, V. E. (2001). Implications for the formation of the Hollywood Basin from gravity interpretations of the northern Los Angeles Basin, California. *US Geological Survey, Open File Report*, 394. <https://pubs.usgs.gov/of/2001/0394/>.
- Irwin, W. (1990). Geologic and plate-tectonic development in the San Andreas fault system. *USGS Professional Paper 1515*, 61–82. Retrieved from <https://pubs.usgs.gov/pp/1990/1515/pp1515.pdf>

- Karato, S., & Jung, H. (1998). Water, partial melting and the origin of the seismic low velocity and high attenuation zone in the upper mantle. *Earth and Planetary Science Letters*, *157*(3–4), 193–207. [https://doi.org/10.1016/S0012-821X\(98\)00034-X](https://doi.org/10.1016/S0012-821X(98)00034-X)
- Kimbrough, D. L., Grove, M., & Morton, D. M. (2015). Timing and significance of gabbro emplacement within two distinct plutonic domains of the Peninsular Ranges batholith, southern and Baja California. *GSA Bulletin*, *127*(1-2), 19-37. <https://doi.org/10.1130/B30914.1>
- Langenheim, V. E., & Jachens, R. C. (2003). Crustal structure of the Peninsular Ranges batholith from magnetic data: Implications for Gulf of California rifting. *Geophysical Research Letters*, *30*(11). <https://doi.org/10.1029/2003GL017159>
- Langston, C. A. (1977). Corvallis, Oregon, crustal and upper mantle receiver structure from teleseismic P and S waves. *Bulletin of the Seismological Society of America*, *67*(3), 713–724.
- Langston, C. A. (1979). Structure under Mount Rainier, Washington, inferred from teleseismic body waves. *Journal of Geophysical Research*, *84*(B9), 4749–4762. <https://doi.org/10.1029/JB084iB09p04749>
- Lee, E. J., Chen, P., Jordan, T. H., Maechling, P. B., Denolle, M. A., & Beroza, G. C. (2014). Full-3-D tomography for crustal structure in southern California based on the scattering-integral and the adjoint-waveform methods. *Journal of Geophysical Research: Solid Earth*, *119*, 6421–6451. <https://doi.org/10.1002/2014JB011346>
- Li, G., Niu, F., Yang, Y., & Tao, K. (2019). Joint inversion of Rayleigh wave phase velocity, particle motion, and teleseismic body wave data for sedimentary structures. *Geophysical Research Letters*, *46*, 6469–6478. <https://doi.org/10.1029/2019GL082746>
- Ligorria, J. P., & Ammon, C. J. (1999). Iterative deconvolution and receiver-function estimation. *Bulletin of the Seismological Society of America*, *89*(5), 1395–1400.
- Lin, F.-C., Moschetti, M. P., & Ritzwoller, M. H. (2008). Surface wave tomography of the western United States from ambient seismic noise: Rayleigh and Love wave phase velocity maps. *Geophysical Journal International*, *173*(1), 281–298. <https://doi.org/10.1111/j.1365-246X.2008.03720.x>
- Lin, F.-C., Tsai, V. C., & Schmandt, B. (2014). 3-D crustal structure of the western United States: Application of Rayleigh-wave ellipticity extracted from noise cross-correlations. *Geophysical Journal International*, *198*(2), 656–670. <https://doi.org/10.1093/gji/ggu160>
- Lin, G. (2020). Spatiotemporal variations of in situ Vp/Vs ratio within the Salton Sea Geothermal Field, southern California. *Geothermics*, *84*, 101740. <https://doi.org/10.1016/j.geothermics.2019.101740>
- Lin, G., & Shearer, P. (2007). Estimating local Vp/Vs ratios within similar earthquake clusters. *Bulletin of the Seismological Society of America*, *97*(2), 379-388. <https://doi.org/10.1785/0120060115>

- Lin, G., Shearer, P. M., Hauksson, E., & Thurber, C. H. (2007). A three-dimensional crustal seismic velocity model for southern California from a composite event method. *Journal of Geophysical Research: Solid Earth*, 112(B11). <https://doi.org/10.1029/2007JB004977>
- Lin, G., Thurber, C. H., Zhang, H., Hauksson, E., Shearer, P. M., Waldhauser, F., et al. (2010). A California statewide three-dimensional seismic velocity model from both absolute and differential times. *Bulletin of the Seismological Society of America*, 100(1), 225–240. <https://doi.org/10.1785/0120090028>
- Livers, A. J., Han, L., Delph, J., White-Gaynor, A., Petit, R., Hole, J. A., et al. (2012). Tomographic characteristics of the northern geothermally active rift zone of the Imperial Valley and its rift margins: Salton seismic imaging project (SSIP). *AGU Fall Meet. Abstr.*
- Lutter, W. J., Fuis, G. S., Ryberg, T., Okaya, D. A., Clayton, R. W., Davis, P. M., et al. (2004). Upper crustal structure from the Santa Monica Mountains to the Sierra Nevada, Southern California: Tomographic results from the Los Angeles Regional Seismic Experiment, Phase II (LARSE II). *Bulletin of the Seismological Society of America*, 94(2), 619–632. <https://doi.org/10.1785/0120030058>
- Ma, Y., & Clayton, R. W. (2016). Structure of the Los Angeles Basin from ambient noise and receiver functions. *Geophysical Journal International*, 206(3), 1645–1651. <https://doi.org/10.1093/gji/ggw236>
- Magistrale, H., McLaughlin, K., & Day, S. (1996). A geology-based 3D velocity model of the Los Angeles basin sediments. *Bulletin of the Seismological Society of America*, 86(4), 1161–1166.
- McCaffree Pellerin, C. L., and N.I. Christensen, Interpretation of crustal seismic velocities in the San Gabriel-Mojave region, southern California. *Tectonophysics*, 286, 253-271, 1998
- Mitchell, T. M., & Faulkner, D. R. (2009). The nature and origin of off-fault damage surrounding strike-slip fault zones with a wide range of displacements: A field study from the Atacama fault system, northern Chile. *Journal of Structural Geology*, 31(8), 802-816. <https://doi.org/10.1016/j.jsg.2009.05.002>
- Morton, D. M., & Kennedy, M. P. (2005). Preliminary Geologic Map of the Sage 7.50 Quadrangle, Riverside County, California, (Map No. 2005–1285). United States Geological Survey. Retrieved from <http://pubs.usgs.gov/of/2005/1285/>
- Murphy, J. M., Fuis, G. S., Ryberg, T., Lutter, W. J., Catchings, R. D., & Goldman, M. R. (2010). Detailed P-and S-Wave Velocity Models along the LARSE II Transect, Southern California. *Bulletin of the Seismological Society of America*, 100(6), 3194-3212. <https://doi.org/10.1785/0120090004>
- Ojo, A. O., Ni, S., Xie, J., & Zhao, L. (2019). Further constraints on the shear wave velocity structure of Cameroon from joint inversion of receiver function, Rayleigh wave dispersion and ellipticity measurements. *Geophysical Journal International*, 217(1), 589-619. <https://doi.org/10.1093/gji/ggz008>

- Park, J., & Levin, V. (2016). Anisotropic shear zones revealed by backazimuthal harmonics of teleseismic receiver functions. *Geophysical supplements to the monthly notices of the Royal Astronomical Society*, 207(2), 1216–1243. <https://doi.org/10.1093/gji/ggw323>
- Plesch, A., Shaw, J. H., Benson, C., Bryant, W. A., Carena, S., Cooke, M., et al. (2007). Community fault model (CFM) for southern California. *Bulletin of the Seismological Society of America*, 97(6), 1793–1802. <https://doi.org/10.1785/0120050211>
- Qiu, H., Lin, F. C., & Ben-Zion, Y. (2019). Eikonal tomography of the Southern California plate boundary region. *Journal of Geophysical Research: Solid Earth*, 124(9), 9755–9779. <https://doi.org/10.1029/2019JB017806>
- Roy, C., & Romanowicz, B. A. (2017). On the implications of a priori constraints in transdimensional Bayesian inversion for continental lithospheric layering. *Journal of Geophysical Research: Solid Earth*, 122, 10,118–10,131. <https://doi.org/10.1002/2017JB014968>
- Sauber, J., Thatcher, W., & Solomon, S. C. (1986). Geodetic measurement of deformation in the central Mojave Desert, California. *Journal of Geophysical Research: Solid Earth*, 91(B12), 12683–12693. <https://doi.org/10.1029/JB091iB12p12683>
- Schmandt, B., & Humphreys, E. (2010). Seismic heterogeneity and small-scale convection in the southern California upper mantle. *Geochemistry, Geophysics, Geosystems*, 11, Q05004. <https://doi.org/10.1029/2010GC003042>
- Schulte-Pelkum, V., & Mahan, K. H. (2014a). A method for mapping crustal deformation and anisotropy with receiver functions and first results from USArray. *Earth and Planetary Science Letters*, 402, 221–233.
- Schulte-Pelkum, V., & Mahan, K. H. (2014b). Imaging faults and shear zones using receiver functions. *Pure and Applied Geophysics*, 171(11), 2967–2991. <https://doi.org/10.1007/s00024-014-0853-4>
- Schulte-Pelkum, V., Mahan, K. H., Shen, W., & Stachnik, J. C. (2017). The distribution and composition of high-velocity lower crust across the continental US: Comparison of seismic and xenolith data and implications for lithospheric dynamics and history. *Tectonics*, 36, 1455–1496. <https://doi.org/10.1002/2017TC004480>
- Shaw, J. H., Plesch, A., Tape, C., Suess, M. P., Jordan, T. H., Ely, G., ... & Olsen, K. (2015). Unified structural representation of the southern California crust and upper mantle. *Earth and Planetary Science Letters*, 415, 1–15. <https://doi.org/10.1016/j.epsl.2015.01.016>
- Shearer, P. M. (1988). Cracked media, Poisson's ratio and the structure of the upper oceanic crust. *Geophysical Journal International*, 92(2), 357–362. <https://doi.org/10.1111/j.1365-246X.1988.tb01149.x>
- Shen, W., & Ritzwoller, M. H. (2016). Crustal and uppermost mantle structure beneath the United States. *Journal of Geophysical Research: Solid Earth*, 121, 4306–4342. <https://doi.org/10.1002/2016JB012887>

- Shen, W., Ritzwoller, M. H., Schulte-Pelkum, V., & Lin, F. C. (2012). Joint inversion of surface wave dispersion and receiver functions: A Bayesian Monte-Carlo approach. *Geophysical Journal International*, *192*(2), 807–836. <https://doi.org/10.1093/gji/ggs050>
- Süss, M. P., & Shaw, J. H. (2003). P wave seismic velocity structure derived from sonic logs and industry reflection data in the Los Angeles basin, California. *Journal of Geophysical Research: Solid Earth*, *108*(B3). <https://doi.org/10.1029/2001JB001628>
- Taborda, R., Azizzadeh-Roodpish, S., Khoshnevis, N., & Cheng, K. (2016). Evaluation of the southern California seismic velocity models through simulation of recorded events. *Geophysical Journal International*, *205*(3), 1342–1364. <https://doi.org/10.1093/gji/ggw085>
- Tanimoto, T., & Prindle Sheldrake, K. (2002). Three-dimensional S-wave velocity structure in southern California. *Geophysical Research Letters*, *29*(8), 1223. <https://doi.org/10.1029/2001GL013486>
- Tape, C., Liu, Q., Maggi, A., & Tromp, J. (2010). Seismic tomography of the southern California crust based on spectral-element and adjoint methods. *Geophysical Journal International*, *180*(1), 433–462. <https://doi.org/10.1111/j.1365-246X.2009.04429.x>
- Vidale, J. E., & Helmberger, D. V. (1988). Elastic finite-difference modeling of the 1971 San Fernando, California earthquake. *Bulletin of the Seismological Society of America*, *78*(1), 122–141.
- Vinnik, L. P. (1977). Detection of waves converted from P to SV in the mantle. *Physics of the Earth and Planetary Interiors*, *15*(1), 39–45. [https://doi.org/10.1016/0031-9201\(77\)90008-5](https://doi.org/10.1016/0031-9201(77)90008-5)
- Water Replenishment District of Southern California (2017), Regional Groundwater Monitoring Report Central Basin and West Coast Basin Los Angeles County, California <https://www.wrd.org/sites/pr/files/2015-16%20RGWMR%20Final.pdf>
- Ward, K. M., & Lin, F. C. (2018). Lithospheric structure across the Alaskan cordillera from the joint inversion of surface waves and receiver functions. *Journal of Geophysical Research: Solid Earth*, *123*(10), 8780–8797. <https://doi.org/10.1029/2018JB015967>
- Wetmore, P. H., Herzig, C., Alsleben, H., Sutherland, M., Schmidt, K. L., Schultz, P. W., ... & Kimbrough, D. L. (2003). Mesozoic tectonic evolution of the Peninsular Ranges of southern and Baja California. *SPECIAL PAPERS-GEOLOGICAL SOCIETY OF AMERICA*, *374*, 93-116.
- Wills, C. J., & Clahan, K. B. (2006). Developing a map of geologically defined site-condition categories for California. *Bulletin of the Seismological Society of America*, *96*(4A), 1483-1501. <https://doi.org/10.1785/0120050179>
- Yang, J., & Sato, T. (2000). Interpretation of seismic vertical amplification observed at an array site. *Bulletin of the Seismological Society of America*, *90*(2), 275-285. <https://doi.org/10.1785/0119990068>

- Yeck, W. L., Sheehan, A. F., & Schulte-Pelkum, V. (2013). Sequential H- κ stacking to obtain accurate crustal thicknesses beneath sedimentary basins. *Bulletin of the Seismological Society of America*, 103(3), 2142–2150. <https://doi.org/10.1785/0120120290>
- Zaitsev, V. Y., Radostin, A. V., Pasternak, E., & Dyskin, A. (2017). Extracting real-crack properties from non-linear elastic behaviour of rocks: abundance of cracks with dominating normal compliance and rocks with negative Poisson ratios. *Nonlinear Processes in Geophysics*, 24(3), 543. <https://doi.org/10.5194/npg-24-543-2017>
- Zhang, Q., & Lin, G. (2014). Three-dimensional Vp and Vp/Vs models in the Coso geothermal area, California: Seismic characterization of the magmatic system. *Journal of Geophysical Research: Solid Earth*, 119(6), 4907–4922. <https://doi.org/10.1002/2014JB010992>